

# Comparative study of manufacturing techniques for coronagraphic binary pupil masks: masks on substrates and free-standing masks

Keigo ENYA,<sup>1</sup> Kanae HAZE,<sup>1</sup> Takayuki KOTANI,<sup>1</sup> and Lyu ABE<sup>2</sup>

<sup>1</sup>*Department of Infrared Astrophysics, Institute of Space and Astronautical Science,  
Japan Aerospace Exploration Agency Yoshinodai 3-1-1, Sagami-hara, Kanagawa 229-8510*

<sup>2</sup>*Laboratoire Universitaire d'Astrophysique de Nice, UMR 6525, Parc Valrose, F-06108 Nice, France  
enya@ir.isas.jaxa.jp*

(Received ; accepted )

## Abstract

We present a comparative study of the manufacture of binary pupil masks for coronagraphic observations of exoplanets. A checkerboard mask design, a type of binary pupil mask design, was adopted, and identical patterns of the same size were used for all the masks in order that we could compare the differences resulting from the different manufacturing methods. The masks on substrates had aluminum checkerboard patterns with thicknesses of 0.1/0.2/0.4/0.8/1.6 $\mu\text{m}$  constructed on substrates of BK7 glass, silicon, and germanium using photolithography and chemical processes. Free-standing masks made of copper and nickel with thicknesses of 2/5/10/20 $\mu\text{m}$  were also realized using photolithography and chemical processes, which included careful release from the substrate used as an intermediate step in the manufacture. Coronagraphic experiments using a visible laser were carried out for all the masks on BK7 glass substrate and the free-standing masks. The average contrasts were  $8.4 \times 10^{-8}$ ,  $1.2 \times 10^{-7}$ , and  $1.2 \times 10^{-7}$  for the masks on BK7 substrates, the free-standing copper masks, and the free-standing nickel masks, respectively. No significant correlation was concluded between the contrast and the mask properties. The high contrast masks have the potential to cover the needs of coronagraphs for both ground-based and space-borne telescopes over a wide wavelength range. Especially, their application to the infrared space telescope, SPICA, is appropriate.

**Key words:** instrumentation: high angular resolution—telescopes—stars: planetary systems

## 1. Introduction

The direct detection and spectroscopy of exoplanets is expected to play an essential role in the understanding of how planetary systems were born, how they evolve, and, ultimately, in finding biological signatures on these planets. For the direct observation of exoplanets, the enormous contrast in luminosity between the central star and the planet is a critical difficulty. For example, the contrast between the sun and the earth observed from outside is  $\sim 10^{-10}$  at visible light wavelengths and  $\sim 10^{-6}$  in the mid-infrared wavelength region, respectively (Traub & Jucks 2002). Therefore, the number of exoplanets detected directly is quite a lot smaller than the number of those detected by other methods (e.g., Mayor & Queloz 1995; Charbonneau et al. 2000), though the first direct observation was finally achieved (e.g., Marois et al. 2008; Kalas et al. 2008; Lagrange et al. 2010). Coronagraphs, which were first developed for solar observations (Lyot 1939), is special optics to reduce the contrast. It is considered that advanced coronagraphs have the potential to make possible further extended direct observations of exoplanets.

Among the various current coronagraphic methods, coronagraphs using binary pupil masks have some advantages, and has been studied (Jacquinot & Roizen-Dossier 1964; Spergel 2001; Vanderbei, Kasdin, & Spergel 2003a; Vanderbei, Spergel, & Kasdin 2003b; Vanderbei, Kasdin, & Spergel 2004; Kasdin et al. 2005a; Kasdin et al. 2005b; Belikov et al. 2007; Enya et al. 2007; Enya et al. 2008; Haze 2009; Enya & Abe 2010; Carlotti, Vanderbei, & Kasdin 2011; Haze 2011; Enya et al. 2011a; Haze 2012). The function of a binary pupil mask coronagraph to produce a high contrast point spread function (PSF) is so less sensitive to wavelength (except the effect of scaling the size of the PSF), and also be quite less sensitive to telescope pointing errors than other coronagraphs. Simplicity is another advantage of this optics. Because of these advantages, the use of a binary pupil mask coronagraph is being considered (e.g., Enya et al. 2011b) for the Space Infrared Telescope for Cosmology and Astrophysics (SPICA) mission (e.g., Nakagawa et al. 2009).

For the development of a binary pupil mask coronagraph, both free-standing masks and masks constructed on substrates are possible. In laboratory demonstration experiments, a high contrast of  $6.7 \times 10^{-8}$  was achieved with a high precision mask constructed on a glass substrate by electron beam lithography (Enya et al. 2008). On the other hand, masks on substrates have undesirable properties. The substrates give rise to transmittance losses, and the applicable wavelength of the coronagraph is limited by the substrate material. Multiple reflections at the front and back surfaces of the mask are another disadvantage.

Considering this background, we carried out a comparative study of mask manufacturing processes. Aluminum (Al) mask patterns of various thicknesses were manufactured on substrates of BK7 glass, silicon (Si), and germanium (Ge). Free-standing masks made of copper (Cu) and nickel (Ni) of various thicknesses were also manufactured. The design of the mask pattern was common to all the masks manufactured so that we were able to carry out a systematic

comparison of the coronagraphic performance focusing on the differences in the manufacturing processes. In this work, we set the primary goal contrast to be  $10^{-6}$  because of the need to observe exoplanets using space infrared telescopes. The design, manufacture, and the results of laboratory tests of the coronagraphic performance are presented in the following sections.

## 2. Mask Design

### 2.1. Checkerboard Pattern

Among the various binary pupil masks for coronagraphs, we chose the checkerboard mask for the following reasons: First, the topology of the checkerboard mask design essentially guarantees the possibility that it can be made as a free-standing mask. Second, the pattern consisting of many rectangular apertures formed of orthogonal straight lines is suitable for our manufacturing processes, rather than other masks consisting of apertures with smooth curves (e.g., Gaussian shaped masks). The design of the checkerboard pattern adopted in this work is shown in Fig.1, in which four dark regions(DRs), DR1–DR4, are produced around the core of the PSF. The contrast, Inner Working Angle(*IWA*), and Outer Working Angle(*OWA*) in the design are  $10^{10}$ ,  $5.4\lambda/D$ , and  $50\lambda/D$ , respectively, in which  $\lambda$  is the wavelength and  $D$  is the length of the diagonal of the whole checkerboard pattern. It should be noted that the LOQO optimizer presented by Vanderbei (1999) was used for optimizing the design.

### 2.2. Variation

Table.1 summarizes the parameters of the various masks used in this work. For the material of the substrate, BK7 glass, Si, Ge were adopted. Masks on BK7 glass substrates are convenient as they can be tested with a visible light source at ambient temperature in air. Such tests for the masks on Si or Ge substrates are not possible because Si and Ge are opaque in the visible light wavelength region. On the other hand, masks on Si and Ge substrates can potentially be used in the mid-infrared wavelength region. The mask pattern was formed in aluminum(Al) of various thicknesses on all of these substrates. The thicknesses were 0.1/0.2/0.4/0.8/1.6 $\mu\text{m}$ . The free-standing masks were manufactured in various thicknesses of either Cu or Ni. We considered high precision manufacture with Cu is more common and established than Ni. On the other hand, Ni is physically tougher and more resistant to oxidation than Cu. The thicknesses of the free-standing masks were 2/5/10/20 $\mu\text{m}$ .

### 2.3. Geometry

The geometry of the masks is shown in Fig.2. The geometry of the substrates was determined by the availability of those suitable for our manufacturing process. As a result,  $\phi$  30mm BK7 glass substrates, and 50mm-square Si and Ge substrates were selected. For all the masks on substrates, the checkerboard pattern was located at the center of the substrate. The whole geometry of the free-standing masks was designed in order to realize actually free-

standing and to make realistic holding possible. As the result, we adopted a 50mm-square design with thicker holding area around the checkerboard pattern area. A goal thickness of the holder area in design is  $\geq 100\mu\text{m}$ .

### 3. Manufacturing processes

#### 3.1. Photo-mask for micro-structure patterning

First, a photo-mask was manufactured on a special glass substrate, which was used the master pattern of micro-structure of all the coronagraphic masks manufactured in this work. Details of the manufacturing process for the photo-mask are shown below, and also in Fig.3.

1. A special 4-inch (101.6mm) square glass plate is used as the substrate
2. The substrate is coated with  $Cr + Cr_2O_3$  ( $0.1\ \mu\text{m}$  thickness) by sputtering, a process in which a thin layer of metal is deposited by momentum exchange between energetic ions in a plasma and the atoms in a target material.
3. A  $0.5\mu\text{m}$  thick layer of photoresist is spin coated on the  $Cr_2O_3$  layer. This procedure is used to make a uniform thin layer of photoresist on the substrate by rotating the substrate at high speed in order to spread the resist by centrifugal force.
4. Exposure: the micro-structure pattern is transferred to the photoresist using a laser(412nm wavelength). Development: the photoresist (positive type) is removed.
5. The substrate is wet etched in an acid etch solution in a thin polyvinyl container.
6. The resist is stripped using a remover.

#### 3.2. Masks on substrate

Next, the masks on substrates were manufactured.  $\phi$  30mm BK7 glass substrates, and 50mm-square Si and Ge substrates were used. The detailed manufacturing process is shown below, and also in Fig.4. Manufacture of the two masks, #SA004S and #SA008S, failed and therefore these masks were not provided to the microscope check in the laboratory tests described in the nest section. The manufactured masks are shown in Fig.6.

1.  $\phi$  30mm BK7 glass, 50mm-square Si, and 50mm-square Ge are used as the substrates
2. Aluminum with thicknesses of  $0.1/0.2/0.4/0.8/1.6\mu\text{m}$  is deposited on the substrates by EB vapor deposition, a process in which the aluminum is heated by an electron beam.
3. Photoresist with a thickness of  $0.1\ \mu\text{m}$  is spin coated on the Al.
4. Exposure: the pattern is transferred from the photo-mask to the photo-resist by UV light (365nm wavelength) exposure. Development: The photoresist (positive type) is removed.
5. The substrate is wet etched in an acid etch solution in a thin polyvinyl container.
6. The photoresist is stripped by dipping in acetone.

### 3.3. Free-standing masks

Lastly, the free-standing masks were manufactured. Details of the manufacturing process of free-standing masks of Cu are given below, and also in Fig.5. The manufacturing process of free-standing masks of Ni are similar. The manufactured masks are shown in Fig.6.

1. A special 4-inch (101.6mm) square glass plate is used as the temporary substrate
2. A sacrificial release layer with a thickness of  $1\ \mu\text{m}$  is spin-coated on the surface.
3. A seed layer of Cu ( $0.5\ \mu\text{m}$  thickness) is deposited by EB vapor deposition on the release layer.
4. Resist (with a goal of  $10\ \mu\text{m}$  thickness) is spin-coated for plating on the Cu substrate.
5. Exposure: the patterns are transferred from the photo-mask to the photo-resist by exposure to UV light (365nm wavelength). Development: the photo-resist is removed (only the illuminated part is dissolved, i.e., the resist is positive type).
6. Cu with goal thicknesses of  $2/5/10/20\ \mu\text{m}$  is grown by electrolytic plating, a process in which metal ions in solution are moved by an electric field to coat an electrode (i.e., the seed layer on the substrate).
7. The substrate is laminated with a dry film resist ( $100\ \mu\text{m}$  thickness) to enable plating to be done for the support structure around the border of the central micro-structure.
8. Exposure: the patterns are transferred from the photomask to the photoresist by UV light exposure (365nm wavelength). Development: the resist (negative type) is removed. Only the illuminated parts of the dry film resist remain.
9. A thick layer of Cu with a goal thickness of  $100\ \mu\text{m}$  is deposited by electrolytic plating.
10. The dry film resist is removed by dipping in acetone.
11. The photoresist is removed by dipping in acetone.
12. The Cu seed layer ( $0.5\ \mu\text{m}$  thickness) is etched by wet etching the substrate in an acid etch solution in a thin polyvinyl container. Not only the seed layer but also  $0.5\ \mu\text{m}$  of Cu is removed in the process.
13. The sacrificial release layer is removed by soaking in acetone.
14. The substrate is rinsed in isopropyl alcohol, then dried naturally.

Achieved thickness of the holder area of the free-standing masks is  $\sim 100\ \mu\text{m}$  and  $\sim 170\ \mu\text{m}$  for Cu and Ni masks, respectively.

This work, comparative study of the mask manufacture, has been requested for several years (e.g., Enya (2008); Enya et al. (2011b)). A free standing mask of an early generation was used in Kotani (2010), and improvement of the manufacture process has been continued. Recently, a free-standing mask having same specification with #FC020 was adopted in Haze (2012). It should be noted that there are confidential details in the manufacturing processes, which are not described in this section explicitly.

## 4. Laboratory tests

### 4.1. Microscope check

The manufactured masks were checked with a digital optical microscope, VHX-90 made by KEYENCE Co. Fig.7 and Fig.8 show examples of the microscope images, cases for a mask on a BK7 glass substrate, #SA016B, and for a free-standing mask, #FC020, respectively. Since the role of the microscope check in this work is a qualifying round for the coronagraphic experiments, simply the topology of the mask was confirmed, rather than quantifying the imperfectness of the shape of many masks, i.e., we checked following: 1) All the holes in the design were reproduced in the manufactured masks. 2) There were no holes unexpected in the design, in the manufactured mask. 3) All the holes in the design were separate from each other in the manufactured mask. All the masks, except #SA004S and #SA008S for which the manufacturing process had failed, passed the microscope check,

### 4.2. Cooling tests

The masks on Si and Ge substrate are designed to be operated at cryogenic temperature, and cooling them to low temperature could potentially delaminate them due to mechanical stresses induced by mismatch of the coefficient of thermal expansion between layers. We therefore carried out cooling tests for the masks on Si and Ge substrate. All masks were installed onto the cold worksurface of a cryostat in vacuum. The worksurface was connected to a liquid nitrogen tank with a thermal strap, and cooled by thermal conduction. The masks were cooled to  $\sim 80\text{K}$  in 10hours (to  $\sim 100\text{K}$  in 2hours), and then warmed up to ambient temperature in 20hours. Lastly microscopic check was applied, and it is confirmed that no delamination was found for all cooled masks.

### 4.3. Coronagraphic experiments

Coronagraphic experiments were carried out on all the masks with BK7 glass substrates and the free-standing masks. The configuration of the experiment is shown in Fig.9, which, except for the masks and their holders, is basically the same as the setup shown in section 2.4 of Haze (2012). The optics were placed in a vacuum chamber, but vacuum pumping was not applied for the experiment presented in this paper. Fig.7 and Fig.8 show examples of a mask installed in the holder, cases for a mask on a BK7 glass substrate, #SA016B, for a free-standing mask, #FC020, respectively. All the coronagraphic images were taken using light passing through the mask (i.e., reflected light was not used). A 632.8nm wavelength He-Ne laser was used as the light source, and this was introduced into the chamber through a single mode fiber. All the focusing and collimation were executed with a plano-convex lens with anti-reflection coatings on both surfaces. A CCD camera set in the chamber was used to take coronagraphic images.  $\times 3.4$  relay optics were set after the focal plane mask to obtain proper image sizes. To realize high dynamic range measurements, the cores and the DRs of the

coronagraphic PSFs were taken separately. For each masks, we evaluated only the DR3 of the four DRs shown in Fig.1 because of consideration for the efficiency of the experiment in this work. The core images were taken with exposure times of 0.03/0.3/3 seconds using two ND filters with a total optical density of 4. The DR of the coronagraphic image was observed with a 300s exposure using a square hole focal-plane mask, without the ND filters. For all images, dark frames were taken with the same configuration, with the same exposure time, but with the light source turned off. The dark frame was subtracted from the corresponding coronagraphic image, and then the raw image of the coronagraphic PSF was obtained.

The observed coronagraphic PSFs for a mask on a BK7 glass substrate, #SA002B, are shown in Fig.10, in which the left and the right panels are the image including the core, and the high sensitivity image of the DR, respectively. The observed coronagraphic PSFs taken with a free-standing mask of Cu, #FC100, are also shown in Fig.11. In both cases, the observed core images are quite similar to the ones expected from the design presented in Fig.1. On the other hand, the observed dark images are filled with irregular speckle patterns. This feature, core images expected from the design and the DR filled with speckle, was commonly found in all the coronagraphic PSFs obtained in this work. Diagonal profiles of the coronagraphic images obtained from the masks with BK7 glass substrates and the free-standing Cu and Ni masks are presented in Fig.12.

For all the masks tested in the coronagraphic experiments, the contrast was derived as the intensity ratio between the peak of the core and the linear average of the DR. The contrasts obtained are presented in Table.2.

## 5. Discussion and Summary

The contrasts obtained are distributed from  $5.3 \times 10^{-8}$  to  $2.1 \times 10^{-7}$ . It should be noted that all the contrasts exceed the goal set at the beginning of this work,  $10^{-6}$ . The average contrasts were  $8.4 \times 10^{-8}$ ,  $1.2 \times 10^{-7}$ , and  $1.2 \times 10^{-7}$  for the masks on BK7 glass substrates, and the free-standing masks of Cu and Ni, respectively. The average contrast for the masks on BK7 glass substrates is higher than those of the free-standing masks. However, because of the dispersion of the data, the statistical significance of this is not valid. Also, significant correlation is not concluded between the contrast and the mask thickness for each of the three types of mask.

Because the contrast in the design is  $10^{-10}$ , it is obvious that there is a practical limiting factor that gives rise to the speckle patterns observed in the DRs. However, identification of this limiting factor was not easy. Using a mask having same specification with #FC020, detail study about the limiting factor was performed as shown in Haze (2012): For example, mask rotation methods were tested. In these tests, it is expected that the speckle patterns are rotated with the mask if the speckle patterns were produced simply by error of the mask shape. However, less correlation was confirmed between the speckle pattern before and after the

mask rotation. Finally suggested candidates of the limiting factor are imperfectness of incident beam(e.g., wavefront error, inhomogeneity of amplitude, and so on) and error in repeatability of the mask position before and after the rotation. Influence of instability of the experimental system is also suggested. For more detail, please see Haze (2012).

The wavefront error, can be corrected by deformable mirrors Trauger & Traub (2007) pioneered ultra high contrast using the wavefront control with High Contrast Imaging Testbed. Using one of early generation of our free-standing mask, Kotani (2010) demonstrated improvement of the contrast by factor of  $\sim 100$  at a part of the dark region close to *IWA* in the air with a visible laser. For the use in infrared wavelength region, development of cryogenic deformable mirror is ongoing. Actuation of a proto-type of Micro Electro Mechanical Systems(MEMS) deformable mirror with 32 actuators were demonstrated at  $\sim 95\text{K}$ (Enya et al. 2009). Toughness tests, vibration tests and rapid pumping tests were also carried out for the proto-type(Enya et al. 2011a).

Coronagraphic experiments for the masks on Ge and Si substrates were not carried out in this work since visible light was used as the light source and the experiments were carried out at ambient temperature in air. Important future work is to demonstrate the coronagraphic performance directly in the mid-infrared wavelength region at cryogenic temperatures in vacuum. Following results, indirectly, suggest applicability of the masks on Ge and Si substrates: 1) The high contrast was achieved using the masks on BK7 glass substrates in this work. 2) The masks on Ge and Si substrates and the masks on BK7 glass substrates were manufactured using same process. 3) The masks on Ge and Si substrates survived the cooling tests. It is also important to evaluate coronagraph using the free-standing masks in infrared at cryogenic temperature. Finally, performance of the all the masks for an infrared coronagraph should be compared.

Only one mask design, a checkerboard type without pupil obscuration, was used in this work to compare the various manufacturing processes. On the other hand, recent progress in mask design allows the binary pupil mask coronagraph to be applied to a normal telescopes with pupil obscuration, which is not specially designed for a coronagraph. Carlotti, Vanderbei, & Kasdin (2011) presented a 2-dimensionally optimized pupil design which provides the ultimate efficiency possible in terms of throughput for a pupil coronagraph mask. An integral 1-dimensional coronagraph pupil mask also gives a higher throughput than conventional ones, and a generalized design of the dark region at the focal plane was introduced to realize a more efficient distribution of the *IWA*, *OWA*, and contrast at the focal plane (Enya & Abe 2010; Enya et al. 2011a). As a result, these high contrast masks have the potential to cover the needs of coronagraphs for ground-based telescopes(e.g., current 8-10m class telescopes like SUBARU, and larger future ones such as TMT, EELT), and space telescopes (e.g., JWST, SPICA) over a wide wavelength region. Indeed, the use of a binary pupil mask coronagraph is planned for the SPICA Coronagraph Instrument(SCI), for which the results of this work are quite encour-

aging. Because of less wavelength dependence of binary pupil mask coronagraphs, it would be worthy to evaluate benefit of applying binary pupil masks for instruments for SPICA for longer wavelength; Mid-infrared Camera and Spectrometer(MCS; Kataza et al. 2010) and/or SPICA FAR-infrared Instrument(SAFARI; e.g., Goicoechea et al. 2012).

In the work presented in this paper, we carried out a comparative study of the manufacturing processes of binary pupil masks for coronagraphs. Both masks on substrates and free-standing masks were manufactured with various materials and thicknesses. Coronagraphic experiments in the visible light region confirmed the high contrast, in which obtained average contrasts were  $8.4 \times 10^{-8}$ ,  $1.2 \times 10^{-7}$ , and  $1.2 \times 10^{-7}$  for the masks on BK7 substrates, the free-standing copper masks, and the free-standing nickel masks, respectively. Significant correlation was not concluded between the contrast and the mask properties. We consider such masks have the potential to cover needs of coronagraphs for various telescopes.

We are grateful to the all pioneers in this field, especially to R. J. Vanderbei. The work is supported by the Japan Society for the Promotion of Science, the Ministry of Education, Culture, Sports, Science and Technology of Japan, and the Japan Aerospace Exploration Agency. We thank A. Suenaga, T. Ishii and their colleagues in Houwa-sangyo Co. and Photoprecision. Co. We also thank to referee's fruitful comments for this paper. Lastly, we would like to express special thanks to S. Tanaka, and wish him well in his current field.

## References

- Carlotti, A., Vanderbei, R., & Kasdin, N. J., 2011, arXiv:1108.4050
- Charbonneau, D., Brown, T. M., Latham, D. W., & Mayor, M. 2000, ApJL, 529, 45
- Belikov, R., Give'on, A., Kern, B., Cady, E., Carr, M., Shaklan, S., Balasubramanian, K., White, V., Echternach, P., Dickie, M., Trauger, J., Kuhnert, A., Kasdin, N. J. 2007, proc. of SPIE, 6693, 66930Y
- Enya, K., Abe, L., Takeuchi, S., Kotani, T., & Yamamuro, T., 2011, Proc. of SPIE, 8146, 81460Q
- Enya, K. et al. 2011, Advances in Space Research, 48, 323
- Enya, K., & SPICA working group 2010, Advances in Space Research, 45, 979
- Enya, K. & Abe, L. 2010, PASJ, 62, 1407
- Enya, K., Kataza, H., & Bierden, P. 2009, PASP, 121, 260
- Enya, K., Abe, L., Tanaka, S., Nakagawa, T., Haze, K., Sato, T., Wakayama, T. 2008, A&A, 461, 783
- Enya, K. 37th COSPAR Scientific Assembly. Held 13-20 July 2008, in Montrèl, Canada., p.812
- Enya, K., Tanaka, S., Abe, L., & Nakagawa, T. 2007, A&A, 480, 899
- Goicoechea, J. R., Roelfsema, P. R., Jellema, W., & Swinyard, B. M. proc. of the 280th Symposium of the IAU held in Toledo, Spain, May 30-June 3, 2011, #179
- Haze, K. 2012, PhD. thesis, arXiv1112.6301H
- Haze, K., Enya, K., Abe, L., Kotani, T., Nakagawa, T., Sato, T., Yamamuro, T. 2011, PASJ, 63, 873

- Haze, K., Enya, K., Abe, L., Tanaka, S., Nakagawa, T., Sato, T., Wakayama, T., Yamamuro, T. 2009, *Advances in Space Research*, 43, 181
- Jacquinet, P., & Roizen-Dossier, B. 1964, *Prog. Opt.*, 3, 29
- Kalas, P., Graham, J. R., Chiang, E., Fitzgerald, M. P., & Clampin, M. 2008, *Science*, 322, 1345
- Kataza, H., Wada, T., Ikeda, Y., Fujishiro, N., Kobayashi, N., & Sakon, I. 2010, *proc. of SPIE*, 7731, 77314A
- Kasdin, N. J., Vanderbei, R. J., Littman, M. G. & Spergel, D. N. 2005, *Appl. Opt.*, 44, 1117
- Kasdin, N. J., Belikov, R., Beall, J., Vanderbei, R. J. Littman, M. G., Carr, M., & Give'on, A. 2005, *Proc. of SPIE*, 5905, 128
- Lagrange, A.-M., Bonnefoy, M., Chauvin, G., Apai, D., Ehrenreich, D., Boccaletti, A., Gratadour, D., Rouan, D., Mouillet, D., Lacour, S., & Kasper, M. 2010, *Science*, 329, 57L
- Lyot, B. 1939, *MNRAS*, 99, 580
- Kotani, T., Enya, K., Nakagawa, T., Abe, L., Miyata, T., Sako, S., Nakamura, T., Haze, K., Higuchi, S., Tange, Y. 2010, *Proc. of a workshop held 14 to 18 September 2009 in Barcelona, Spain*. Edited by Vincent Coudé du Foresto, Dawn M. Gelino, and Ignasi Ribas. San Francisco: Astronomical Society of the Pacific, p.477
- Marois, C., Macintosh, B., Barman, T., Zuckerman, B., Song, I., Patience, J., Lafrenière, D., & Doyon, R. 2008, *Science*, 322, 1348
- Mayor, M., & Queloz, D. 1995, *Nature*, 378, 355
- Nakagawa, T., & Spica Team 2009, *SPICA joint European/Japanese Workshop, held 6-8 July, 2009 at Oxford, United Kingdom*. Edited by A. M. Heras, B. M. Swinyard, K. G. Isaak, and J. R. Goicoechea. EDP Sciences, 2009, p.01001
- Spergel, D. N., 2001, *arXiv:astro-ph/0101142*
- Tanaka, S., Enya, K., Nakagawa, T., Kataza, H., & Abe, L. 2006, *PASJ*, 58, 627
- Traub, W. A., & Jucks, K. W. 2002, *Astro-ph/0205369*
- Trauger, J. T., & Traub, W. A. 2007, *Nature*, 446, 771
- Vanderbei, R. J., Kasdin, N. J. & Spergel, D. N. 2004, *ApJ*, 615, 555
- Vanderbei, R. J., Kasdin, N. J. & Spergel, D. N. 2003, *ApJ*, 590, 593
- Vanderbei, R. J., Spergel, D. N., and Kasdin, N. J., 2003, *ApJ*, 599, 686
- Vanderbei, R. J. 1999, *Optimization methods and software*, 11, 451

**Table 1.** Summary of the mask specifications.

Type	No.	Mask	Thickness( $\mu\text{m}$ )	Substrate	Note
on substrate	#SA001B	Al	0.1	BK7	AR*
	#SA002B	Al	0.2	BK7	AR*
	#SA004B	Al	0.4	BK7	AR*
	#SA008B	Al	0.8	BK7	AR*
	#SA016B	Al	1.6	BK7	AR*
	#SA001S	Al	0.1	Si	CL <sup>†</sup>
	#SA002S	Al	0.2	Si	CL <sup>†</sup>
	#SA004S	Al	0.4	Si	Failed <sup>‡</sup>
	#SA008S	Al	0.8	Si	Failed <sup>‡</sup>
	#SA016S	Al	1.6	Si	CL <sup>†</sup>
	#SA001G	Al	0.1	Ge	CL <sup>†</sup>
	#SA002G	Al	0.2	Ge	CL <sup>†</sup>
	#SA004G	Al	0.4	Ge	CL <sup>†</sup>
	#SA008G	Al	0.8	Ge	CL <sup>†</sup>
	#SA016G	Al	1.6	Ge	CL <sup>†</sup>
Free-standing	#FC020	Cu	2	—	
	#FC050	Cu	5	—	
	#FC100	Cu	10	—	
	#FC200	Cu	20	—	
	#FN020	Ni	2	—	
	#FN050	Ni	5	—	
	#FN100	Ni	10	—	
	#FN200	Ni	20	—	

\* Anti-reflection coatings were applied to both sides.

<sup>†</sup> Cooling tests were applied.

<sup>‡</sup> Manufacturing failed.

**Table 2.** Contrast obtained by experiment.

No.	Contrast	No.	Contrast	No.	Contrast
#SA001B	$6.6 \times 10^{-8}$	#FC020	$2.1 \times 10^{-7}$	#FN020	$1.1 \times 10^{-7}$
#SA002B	$1.1 \times 10^{-7}$	#FC050	$5.3 \times 10^{-8}$	#FN050	$8.5 \times 10^{-8}$
#SA004B	$5.9 \times 10^{-8}$	#FC100	$1.1 \times 10^{-7}$	#FN100	$1.2 \times 10^{-7}$
#SA008B	$7.3 \times 10^{-8}$	#FC200	$9.3 \times 10^{-8}$	#FN200	$1.8 \times 10^{-7}$
#SA016B	$1.1 \times 10^{-7}$				
Average	$8.4 \times 10^{-8}$		$1.2 \times 10^{-2}$		$1.2 \times 10^{-7}$

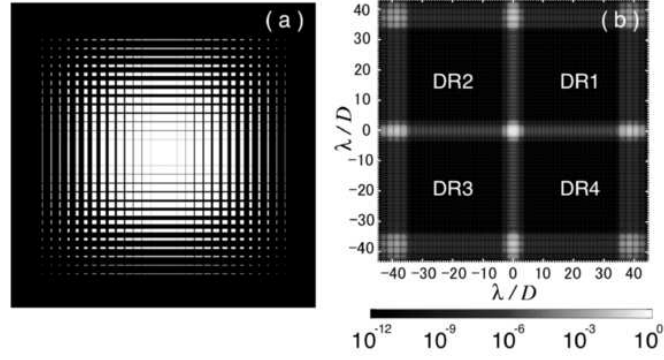


**Fig. 1.** Mask design. Left: design of the pupil mask. Optical transmittances of the black and white areas are 0 and 1, respectively. Right: simulated PSF. Four dark regions(DRs), DR1-DR4, are produced around the core of the PSF.

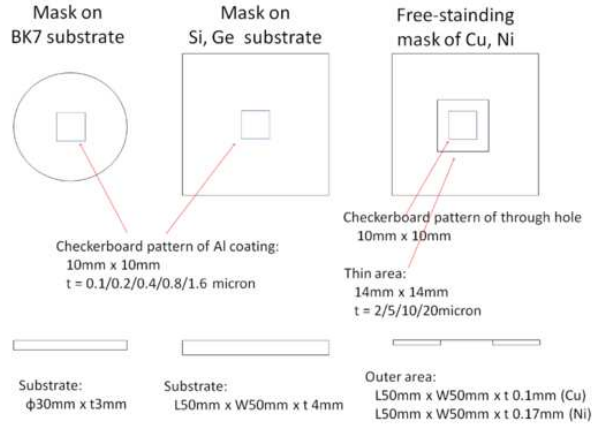


**Fig. 2.** Geometry of the masks.

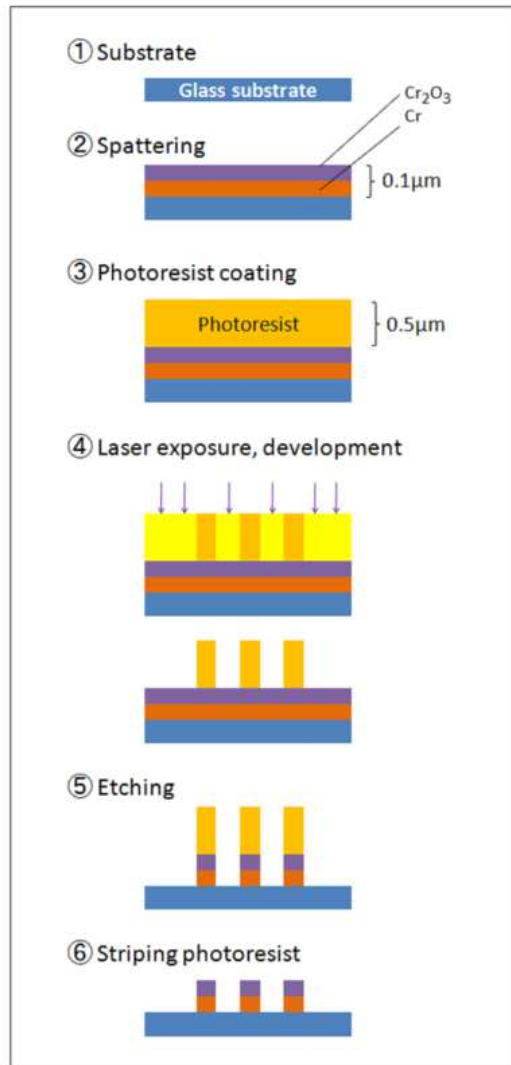


**Fig. 3.** Manufacturing process of the photomask.

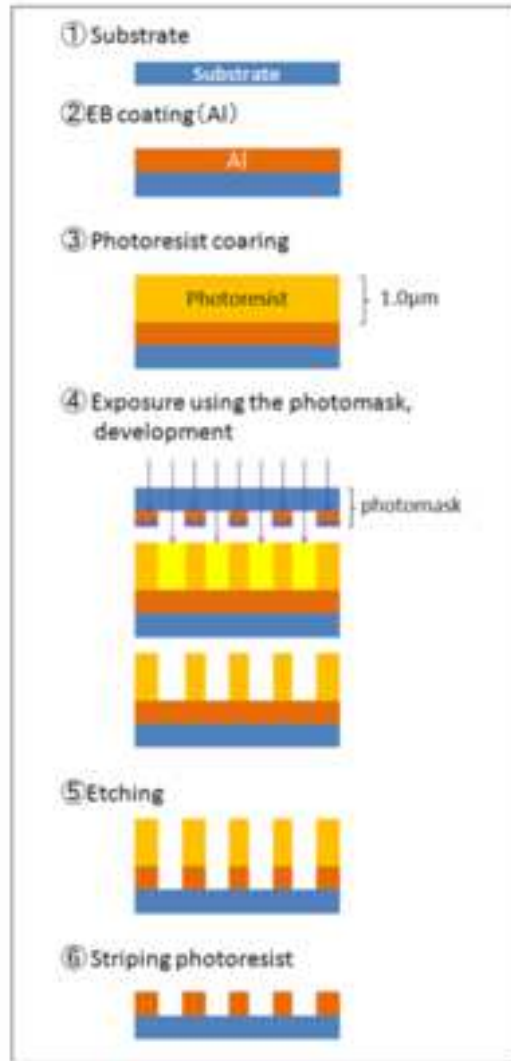


Fig. 4. Manufacturing process of masks on substrates.

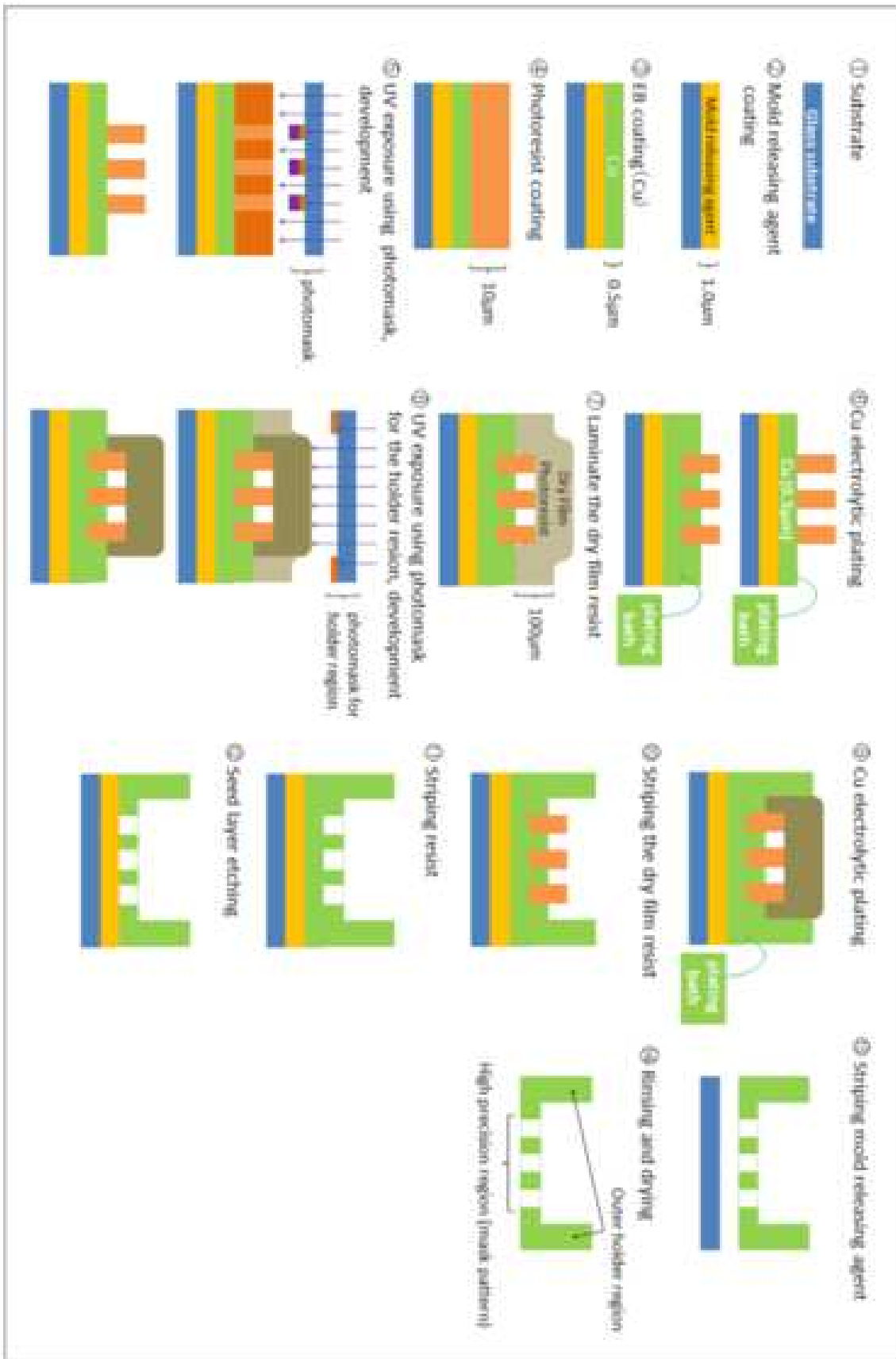
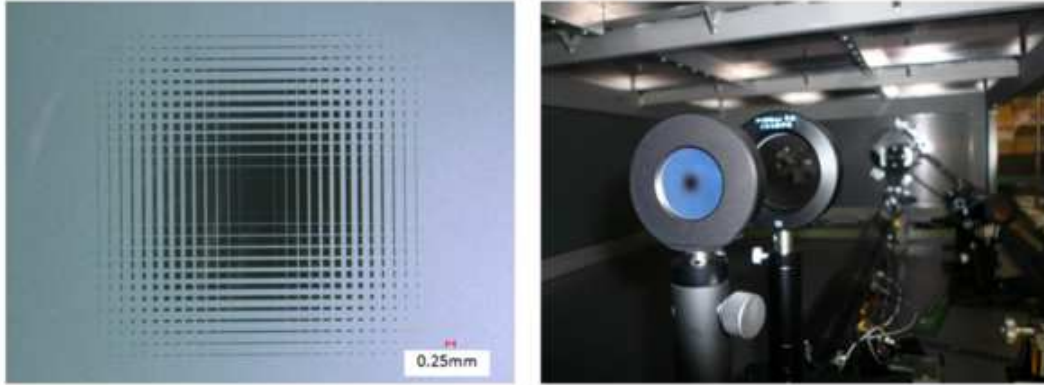


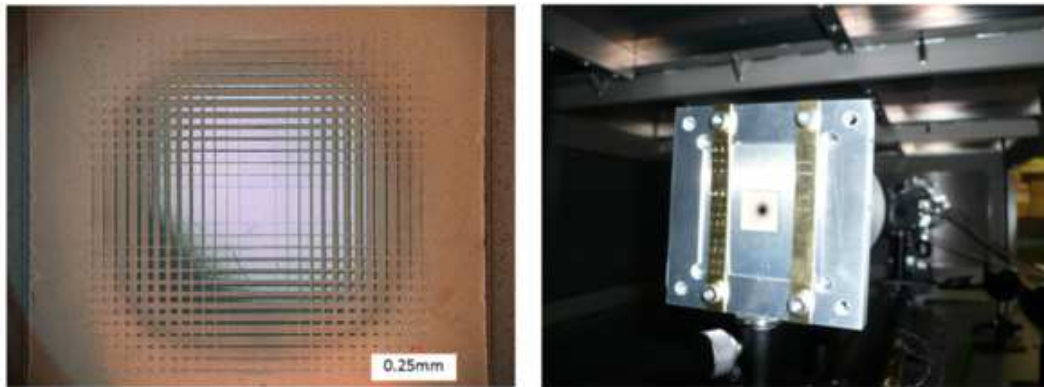
Fig. 5. Manufacturing process of free-standing masks of Cu. Manufacturing process of free-standing masks of Ni are similar.



Fig. 6. Manufactured masks.



**Fig. 7.** Left: microscope image of a mask on a BK7 glass substrate, #SA016B. Right: the mask installed in the holder.



**Fig. 8.** Left: microscope image of a free-standing mask of Cu, #FC020. Right: mask installed in the holder.

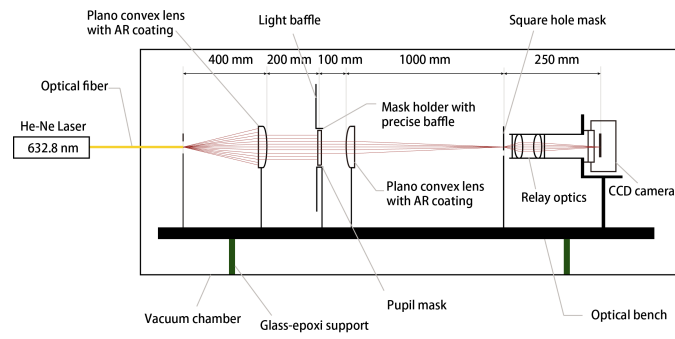


**Fig. 9.** Configuration of the coronagraphic experiment.

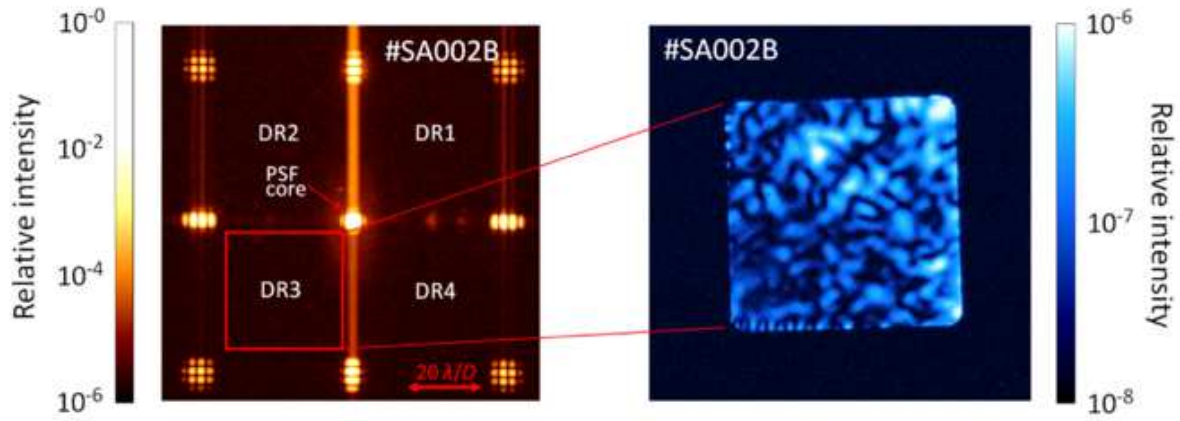


**Fig. 10.** Coronagraphic image taken with a mask on a BK7 glass substrate, #SA002B. Left: image includes the core of the PSF. Right: high sensitivity image of the DR taken with a square hole mask.

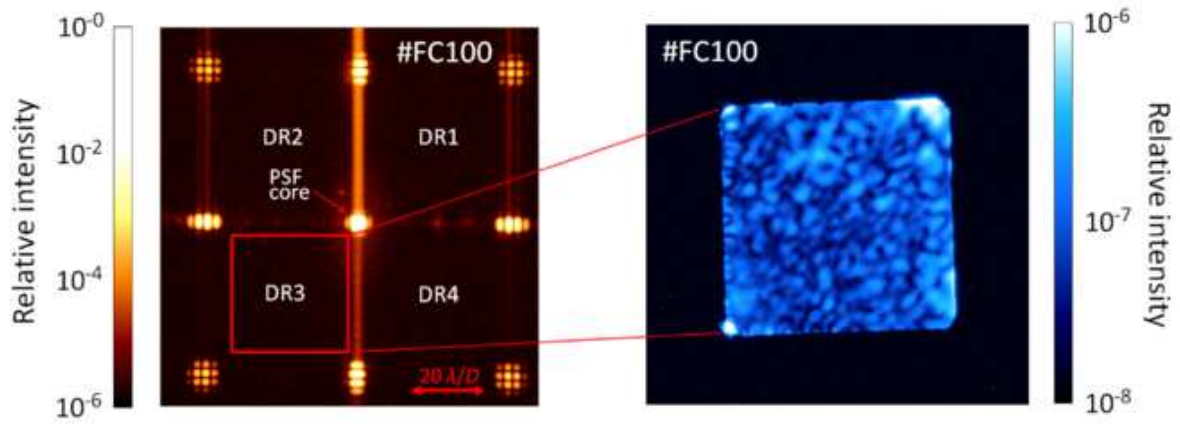


**Fig. 11.** Coronagraphic image taken with a free-standing mask of Cu, #FC100. Left: image includes the core of the PSF. Right: high sensitivity image of the DR taken with a square hole mask.

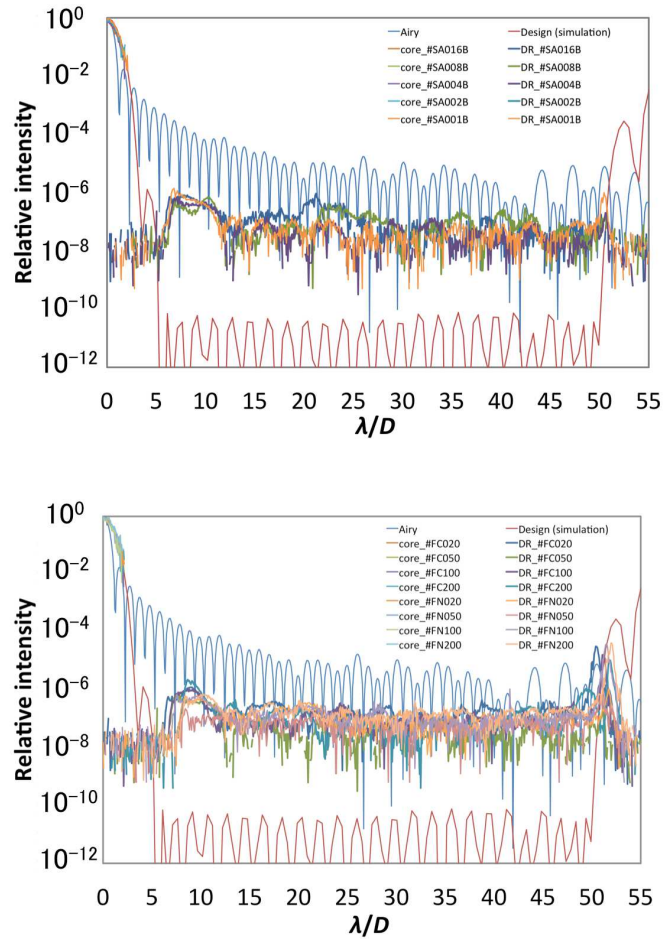


**Fig. 12.** Left: diagonal profiles of coronagraphic images obtained with masks on BK7 substrate. Right: diagonal profiles of coronagraphic images obtained with free-standing masks.